ORIGINAL ARTICLE

Rui Li · Albert J. Shih

Finite element modeling of 3D turning of titanium

Abstract The finite element modeling and experimental valida-
tion of 3D turning of grade two commercially pure titanium are
presented. The Third Wave AdvantEdge machining simulation
software is applied for the finite element modeling. Machin-
ing experiments are conducted. The measured cutting forces and
chip thickness are compared to finite element modeling results
with good agreement. The effects of cutting speed, a limiting
factor for productivity in titanium machining, depth of cut, and
tool cutting edge radius on the peak tool temperature are inves-
tigated. This study explores the use of 3D finite element mod-
eling to study the chip curl. Reasonable agreement is observed
under turning with small depth of cut. The chip segmentation
with shear band formation during the Ti machining process is
investigated. The spacing between shear bands in the Ti chip is
comparable with experimental measurements. Results of this re-
search help to guide the design of new cutting tool materials and
coatings and the studies of chip formation to further advance the
productivity of titanium machining.

Keywords Chip morphology · Machining process ·
3D finite element modeling · Titanium machining

1 Introduction

Titanium (Ti) and its alloys are lightweight, corrosion resis-
tant, and high temperature materials. Titanium has the high-
est strength-weight ratio of all commonly used metals up to
550 °C [1]. Titanium is the ninth most abundant element and the
fourth most abundant metal in earth's crust [2]. However, the ex-
traction and processing cost to produce raw Ti material is high
due to its high free energy for reduction of oxide [2]. The high
cost has limited Ti to the military, aerospace, racing, medical,

R. Li · A.J. Shih (✉)
Mechanical Engineering,
University of Michigan,
Ann Arbor, MI 48109-2125, USA
E-mail: shiha@umich.edu
Fax: +1-734-9360363

and other, applications in which the material cost is not a key
factor.

As reported by Hurless and Froes [1], Kraft [2], and Turner
and Hansen [3], several emerging technologies have been de-
veloped to reduce the cost of producing raw Ti material in recent
years. This has brought about the potential of low cost Ti and
the possibility for automotive applications [4]. While reducing
the material cost can go a long way toward the usage of Ti, the
high machining cost is another major technical barrier that needs
to be overcome. Ti machining has been studied extensively in
the past. Machado and Wallbank [5], Ezugwu and Wang [6],
Yang and Liu [7], and Rahman et al. [8] have reviewed tech-
nologies and barriers associated with Ti machining in articles
published in 1990, 1997, 1999, and 2003, respectively. The high
temperature in a small, concentrated area at the tool tip and
the segmented chip formation with adiabatic shear band due to
thermal-mechanical instability are two major factors that limit
the machinability of Ti. The high tool temperature promotes the
tool diffusion wear and limits the cutting speed. The chip shear
band formation creates the fluctuation in cutting forces and the
associated chipping at tool cutting edges.

The recent research in Ti machining concentrates on studying
the effect of machining process on fatigue life [9, 10], under-
standing the adiabatic shear band formation [11–15], investigat-
ing the cryogenic machining [16], high-speed machining [17–
19], and wear of new tool materials [20]. Yang and Liu [7]
concluded that, to further reduce the cost of effective machin-
ing of Ti, a better understanding of the underlying mechanism
of Ti machining process is necessary through better process and
performance models, thermal modeling, and finite element simu-
lation. Although the 2D modeling of Ti machining has been
studied [14, 15, 21], there is a lack of research in 3D finite elem-
ent modeling, which can provide more detailed information of
the stress, strain, and temperature distributions in the tool and
workpiece, surface integrity of the part, and mechanics of chip
curl. It is the goal of this research to study the 3D finite element
modeling of Ti machining.

Advancements in machining process modeling have demon-
strated the capability to provide reliable predictions of the per-

formance of cutting process and the influence of the process parameters on the product quality [22, 23]. Experiments are conducted to verify 3D finite element simulation results. In this paper, the experimental setup is first introduced. The 3D finite element modeling and comparison of cutting forces and chip thickness with experimental measurements are discussed. Effects of cutting speed and tool edge radius are analyzed. The analysis of chip curl and chip segmentation using 3D finite element modeling is explored.

2 Experimental setup and design

2.1 Experimental setup

The machining experiments were conducted on a Lodge and Shipley 30 HP CNC lathe. The grade two commercially pure (CP) Ti rod, 31.8 mm in diameter, was the work-material used. A left-handed tool holder, Kennametal CTAPL-163D, was used to hold a triangular shape insert. The uncoated WC-Co tool insert, Kennametal TPG322 with 0.8 mm nose radius (denoted as r in Fig. 1a), honed cutting edge, and K313 grade material (1 μm grain size WC in 6% Co matrix), was used in this study. As shown in Fig. 1a, the tool insert fed to the workpiece in the axial direction and reduced the radius of the workpiece by the depth of cut, a. The tool can engage from two sides of the workpiece, illustrated as the right-handed tool and left-handed tool in Fig. 1a. The left-handed tool configuration was used in the experiment. The right-handed tool was the default configuration in 3D finite element modeling.

The tool holder controls the orientation of the tool and workpiece, which is defined by the lead, back rake, and side rake angles in turning [24]. As shown in Fig. 1a, the major cutting edge is perpendicular to the direction of feed, i.e., the lead angle is 0°. As shown in Fig. 1b, the major cutting edge is a single point in the front view; therefore, the back rake angle is 0°. A XYZ coordinate system is defined to show the relative orientation of the tool and cutting forces. The Y-axis is the radial direction, which is parallel to the major cutting edge. The Z-axis is parallel to the axial direction of the cylindrical workpiece. The X-axis is the cutting direction. The side rake angle, as shown in the front view in Fig. 1b, is marked as α. Fig. 1b also shows the relief angle, β. In the study, $\alpha = 5°$ and $\beta = 6°$.

The three measured cutting forces on the tool insert in the X, Y, and Z direction are designated as tangential force (F_t), radial force (F_r), and axial force (F_a), respectively. A Kistler 9257A 3-axis piezoelectric dynamometer was used to measure these three force components. The force signal was processed using the charge amplifiers and recorded by a PC-based data-acquisition system.

2.2 Experiment design

A baseline cutting test with four cutting speeds (24.4, 48.8, 97.5, and 195 m/min) and two feeds (0.254 and 0.381 mm/rev) were conducted at 1.02 mm depth of cut. Cutting forces and chip thickness were measured and compared to 3D finite element simulation results. One additional experiment was performed at small depth of cut (0.254 mm) with 48.8 m/min cutting speed and 0.254 mm/rev feed. All cutting tests were conducted dry without using coolant.
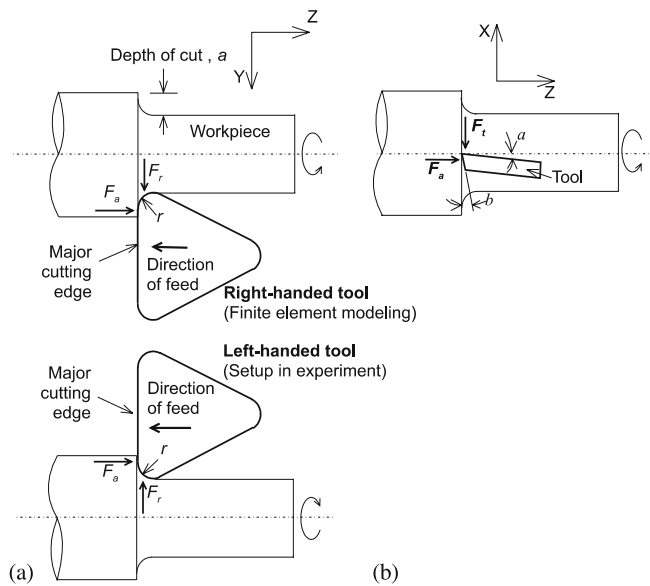
3 Finite element machining model

3.1 3D Finite element machining simulation

The AdvantEdge 3D version 4.5 machining simulation software by Third Wave Systems at Minneapolis, MN was used to model the Ti machining process.

The updated-Lagrangian finite element method with continuous remeshing and adaptive meshing techniques was applied [25]. The coupling of the thermal and mechanical modeling of the tool and workpiece deformation is applied [26]. Figure 2 shows the initial 3D finite element mesh using a tool with nose radius. The XYZ coordinate is defined the same way as in Fig. 1 for the right-handed turning configuration. The 4-node, 12 degree-of-freedom tetrahedral finite element was used to model the workpiece and tool. The whole model includes approximately 100 000 nodes. The top and back surfaces of the tool are fixed in all directions. The workpiece is constrained in vertical (Z) and lateral (Y) directions on the bottom surface and moves at the cutting speed in the horizontal direction ($-X$) toward the stationary tool.

3.2 Material and friction models

The work-material model in finite element analysis contains the power-law strain hardening, thermal softening, and rate sensitiv-

Fig. 1a,b. Schematic diagram of the lathe turning experiment setup with the side rake angle α, relief angle β, tangential force F_t, radial force F_r, and axial force F_a: **a** top view and **b** front view

Fig. 2. Initial finite element mesh for 3D turning model (unit: mm)
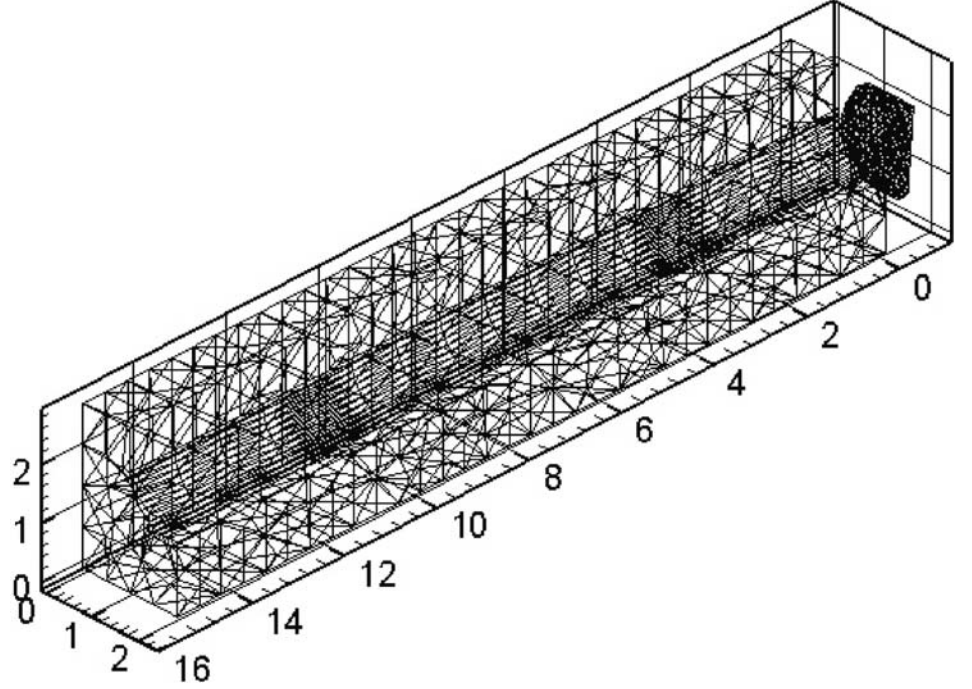
ity [25]. The material behaviors are governed by the following equations:

$$\left(1+\frac{\dot{\varepsilon}^p}{\dot{\varepsilon}_0^p}\right) = \left[\frac{\bar{\sigma}}{g(\varepsilon^p)}\right]^{m_1}, \quad \text{if } \dot{\varepsilon}^p \le \dot{\varepsilon}_t \tag{1}$$

$$\left(1+\frac{\dot{\varepsilon}^p}{\dot{\varepsilon}_0^p}\right)\left[1+\frac{\dot{\varepsilon}_t}{\dot{\varepsilon}_0^p}\right]^{\frac{m_2}{m_1}-1} = \left[\frac{\bar{\sigma}}{g(\varepsilon^p)}\right]^{m_2}, \quad \text{if } \dot{\varepsilon}^p > \dot{\varepsilon}_t \tag{2}$$

$$g(\varepsilon^p) = \sigma_0\theta(T)\left[1+\frac{\varepsilon^p}{\varepsilon_0^p}\right]^{\frac{1}{n}} \tag{3}$$

where $\bar{\sigma}$ is the effective Mises stress, σ_0 is the initial yield stress, ε^p is the plastic strain, $\dot{\varepsilon}^p$ is the plastic strain rate, $\dot{\varepsilon}_0^p$ is the reference plastic strain rate, $\dot{\varepsilon}_t$ is the threshold strain rate, ε_0^p is the reference plastic strain, m_1 and m_2 are the strain rate exponents, and n is the strain hardening exponent.

The $\theta(T)$ in Eq. 3 is determined by:

$$\theta(T) = C_0 + C_1T + C_2T^2 + C_3T^3 + \cdots \quad \text{if } T \le T_{\text{cut}} \tag{4}$$

$$\theta(T) = \theta(T_{\text{cut}}) - \left(\frac{T-T_{\text{cut}}}{T_{\text{melt}}-T_{\text{cut}}}\right) \quad \text{if } T > T_{cut} \tag{5}$$

where $C_0, C_1, \ldots$ are material constants, T_{cut} is the threshold temperature, and T_{melt} is the melting temperature.

All parameters are build-in constants in the material database of the software. Properties of the CP Ti available in the open literature were used [27–29]. The thermal conductivity and heat capacity are assumed to be temperature independent and set as 16.4 W/m K and 523 J/kg °C, respectively. The density, Young's modulus and Poisson's ratio are 4510 kg/m³, 105 GPa, and 0.37, respectively.

Because the Young's modulus of WC-Co is about 631 GPa, which is six times larger than that of CP Ti, the deformation of tool is small. As a result, the WC-Co tool is assumed to be perfectly elastic. One Coulomb coefficient of friction is used across the whole rake face to model the friction at the tool-chip interface.

3.3 Finite element analysis

Nine simulations with the process parameters matched to those of cutting experiments were conducted. Because of the difficulty to accurately measure the tool edge radius, another set of six simulations with three tool edge radii (6.35, 12.7, and 20.0 μm) and two feeds (0.254 and 0.381 mm/rev) were conducted at 195 m/min cutting speed and 1.02 mm depth of cut. The effect of tool edge radius on cutting forces, chip thickness, and tool temperatures are investigated. The initial temperature was 20 °C.

4 Experimental validation of finite element modeling

Figure 3 shows the comparison between the finite element modeling (open symbol) and experimental measured (solid symbol) tangential, radial and axial forces. For the tangential forces F_t, the finite element method generally under-estimated the results. At 0.254 mm/rev feed, the discrepancy ranges from 15% at 24.4 m/min cutting speed to 12% at 195 m/min cutting speed. At 0.381 mm/rev, the discrepancy ranges from 20% at 24.4 m/min cutting speed to 7.6% at 195 m/min cutting speed. For the radial and axial forces (F_r and F_a), the discrepancy is less than 10% between finite element simulation and experimental measurement results.

Fig. 3a,b. Comparison of cutting forces: **a** 0.254 and **b** 0.381 mm/rev feed

(a)

(b)
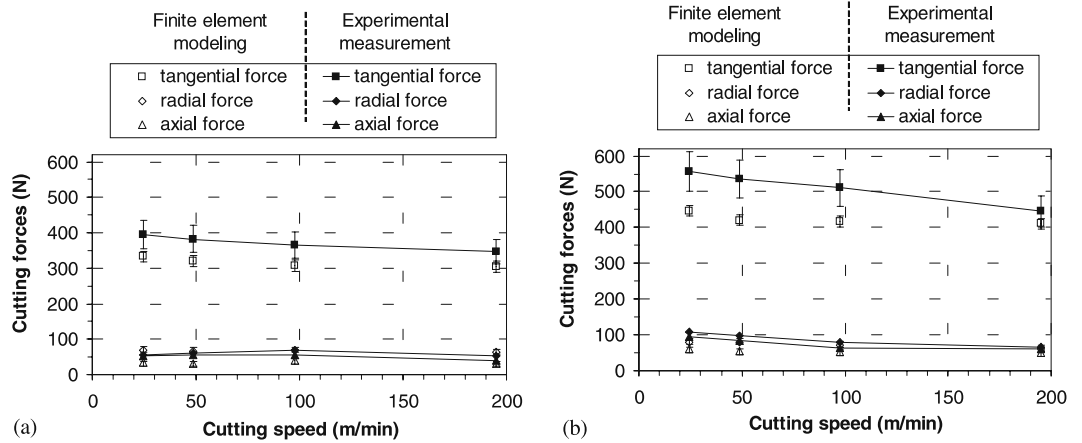
For the cutting at small, 0.254 mm depth of cut (48.8 m/min cutting speed and 0.254 mm/rev feed), the F_t, F_r, and F_a are in the 114–140, 51–71, and 14–30 N range from finite element modeling and 116–130, 51–61, and 16–33 N from experimental measurements, respectively. The finite element method also generally under-estimates the cutting forces. The discrepancy is likely due to the simplified friction model and material properties modeling at low speeds.

Although some discrepancies exist, the cutting force results validate the finite element modeling results and set the direction for further refinement to improve the accuracy in modeling. The feed has significant effect on the cutting force. At high cutting speed, cutting forces were reduced slightly.

Chip thickness is affected by the deformation in the shear zone and friction at the tool workpiece interface. In the experiment, the maximum thickness of the segmented chip at ten random locations is measured using a caliper. The average value is used to represent the chip thickness. In finite element simulation, the chip is oriented to find a band encompassing its cross-section, like the measuring with the caliper, to estimate the chip thickness. The comparison of experimentally measured and finite element estimated chip thickness across different cutting speeds

Fig. 4. Comparison of chip thickness

and feeds is shown in Fig. 4. The agreement is reasonable. The chip thickness increases at larger feed, and decreases slightly at higher cutting speed. The small increase of chip thickness from 24.4 to 48.8 m/min cutting speed at 0.381 mm/rev feed is considered a deviation from the general trend and likely due to the inconsistency of thickness in segmented Ti chips.

5 Finite element investigation of cutting speed and tool edge radius effects

Tool temperature is a key factor that accelerates the tool wear and limits the cutting speed and productivity in Ti machining. Experimental measurement of tool temperature is difficult. On the contrary, the finite element simulation can provide a quick and accurate prediction of the tool temperature under various cutting conditions. The effect of cutting speed on tool temperature is investigated. The sharp cutting edge is also difficult to measure experimentally and is changing during the machining process. The effect of tool edge radius on cutting forces, chip thickness, and peak tool temperature is analyzed.

An example of the tool and workpiece temperature distributions of the nine 3D finite element cutting simulations is shown Fig. 5a. The process parameter for the selected example is 195 m/min cutting speed, 0.254 mm/rev feed, 1.02 mm depth of cut, and 6.35 μm tool edge radius. The chip curl and the engagement of the tool and workpiece are shown in Fig. 5a. Figure 5b shows the tool temperature distribution. The high temperature is concentrated around the straight major cutting edge and the round nose of the tool. The peak temperature is about 480 °C. Figure 5c views the temperature distribution of the chip in the tool-chip contact area. The high temperature, about 510 °C, is concentrated in regions near the nose and major cutting edges with peak temperature slightly higher than that of the tool.
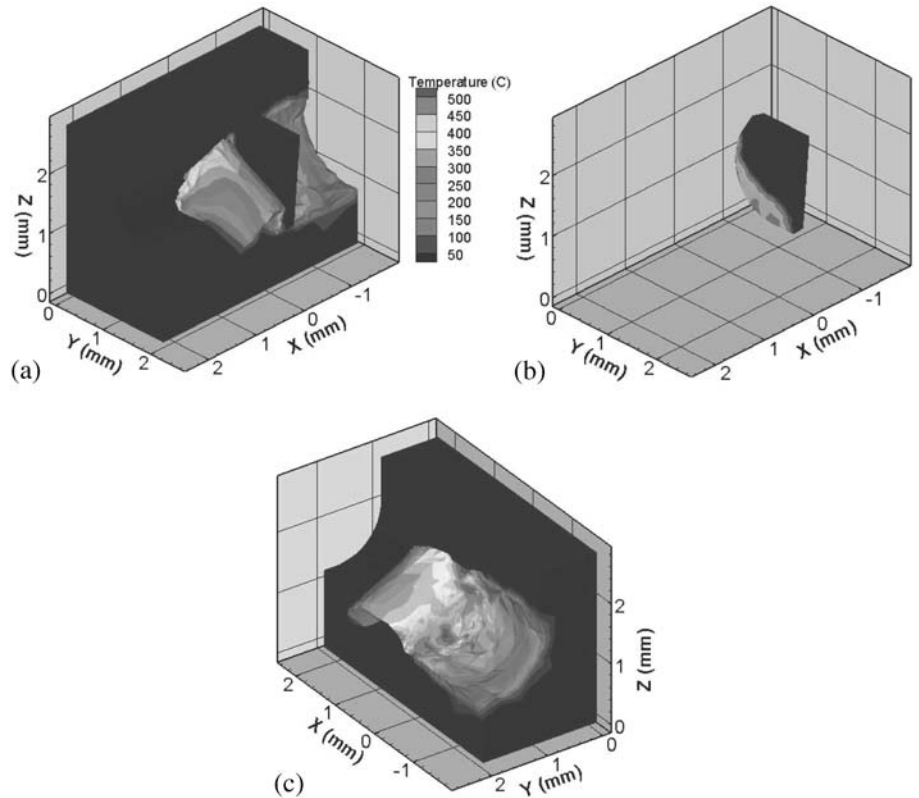
5.1 Effect of cutting speed on tool temperature

Figure 6 shows the peak temperature on the tool rake face of the eight baseline cutting experiments at two feeds and four cutting speeds. The peak tool temperature is independent of the feed.
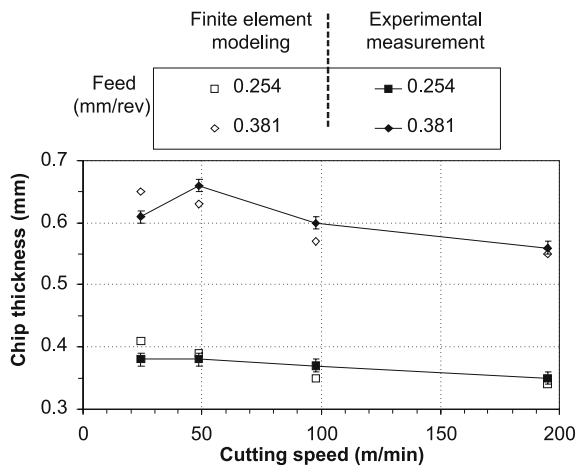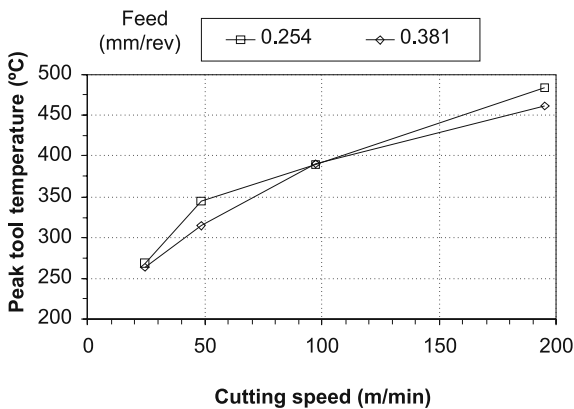
Fig. 5a–c. Temperature distributions: **a** tool, workpiece and chip, **b** tool, and **c** chip

This is comprehensible since the very sharp tool cutting edge radius (6.35 μm) was used. The peak tool temperature increases significantly from about 260 °C at 24.4 m/min cutting speed to 480 °C at 195 m/min, as shown in Fig. 6. This demonstrates the effect of high speed machining on tool temperature.

5.2 Effect of tool edge radius on cutting forces, chip thickness and tool temperature

Six finite element simulations with 6.35, 12.7 to 20.0 μm tool edge radius are conducted at 0.254 and 0.381 mm/rev feed,

195 m/min cutting speed, and 1.02 mm depth of cut. The 6.35 μm represents the ideal, very sharp cutting edge. Results of the cutting forces vs. edge radius are shown in Fig. 7. The feed has a more significant effect on the tangential force and negligible effect on the radial and axial forces. The 0° lead angle and back rake angle is the likely cause of such phenomenon. The resultant cutting force increases at larger edge radius. This is ex-

Fig. 6. Peak tool temperature as a function of cutting speed
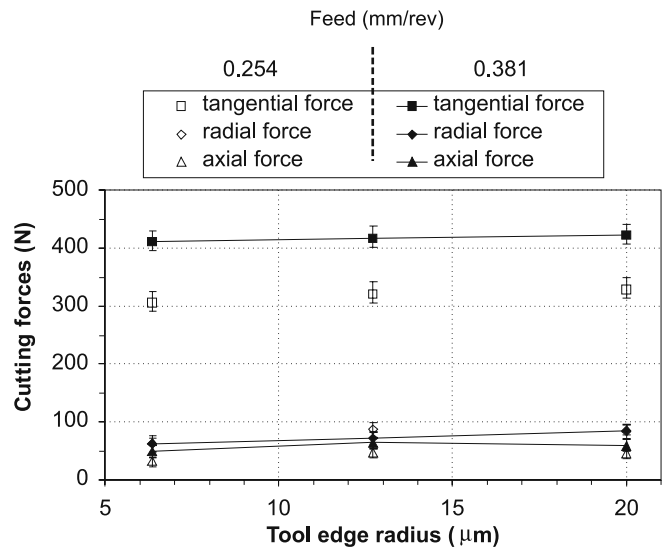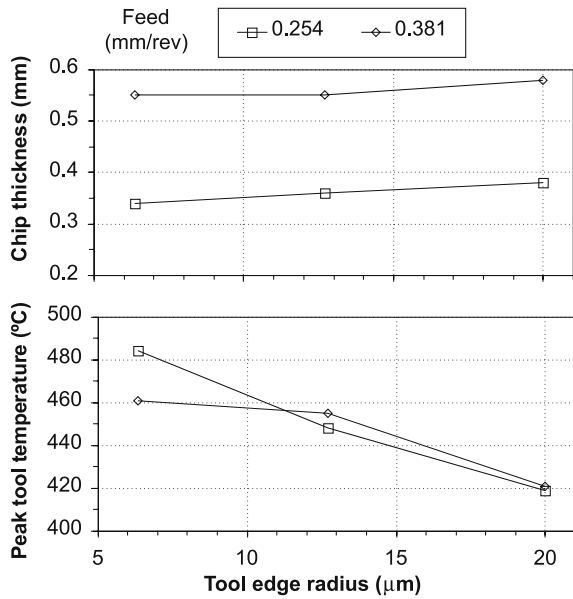

Fig. 7. Cutting forces vs. tool edge radius

Fig. 8. Chip thickness and peak tool temperature vs. tool edge radius

creases with the increasing tool edge radius. When machining Ti, as shown in Fig. 5b and reported in [5], the high tool temperature is concentrated at the very tip of the tool. The heat generated is narrowly concentrated at the very sharp tool tip. This results in the high peak temperature at the tip of tool with small edge radius.

6 Chip curl

This study explores the use of 3D finite element modeling to predict the chip curl in turning. Jawahir and van Luttervelt [30] and Fang [31] have reviewed the past research of chip curl in turning. Two typical types of chip curl are the up-curl, which is a result of velocity variation along the chip thickness [32, 33], and the side-curl, which is caused by the change in velocity across the chip width [33, 34]. In addition, Fang [31] has shown the third pattern of chip lateral-curl. The actual chip curl in turning is the combination of these three patterns. One chip curl pattern may dominate, as will be seen later in experimental observations and finite element simulation results.

Figure 9 shows the experimental and finite element modeling of chip curl in machining of CP Ti with 0.254 mm depth of cut, 48.8 m/min cutting speed, 0.254 mm/rev feed, and 0.8 mm tool nose radius. Figure 9a shows the picture of the chip. The configuration of the chip, tool, and rotational axis of workpiece is shown in Fig. 9b. The top view of the tool and uncut chip cross-section is shown in Fig. 9c. The feed is denoted as f.
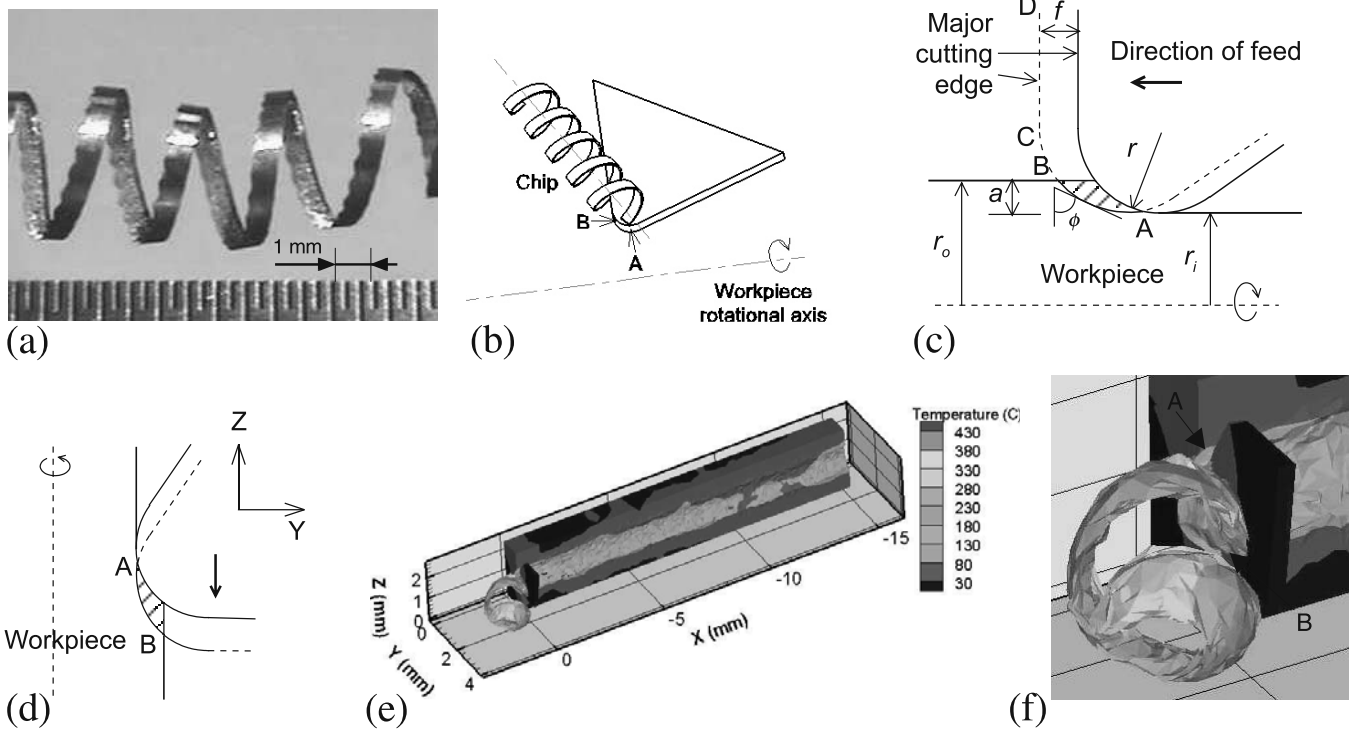
pected since, at a larger tool edge radius, the tool becomes blunt and the material removal is less efficient.

Figure 8 shows the chip thickness and peak tool temperature vs. the tool edge radius. The chip is slightly thicker with larger tool edge radius. The peak tool temperature generally de-

(a)   (b)   (c)

(d)   (e)   (f)

Fig. 9a–f. Chip curl with 0.254 mm depth of cut, 48.8 m/min cutting speed, 0.254 mm/rev feed, and 0.8 mm tool nose radius: **a** tubular chip in the experiment, **b** up-curl dominated chip, left-handed tool, and rotational axis of workpiece, **c** top view of the left-handed tool and uncut chip cross-section, **d** top view of the right-handed tool and uncut chip cross-section, **e** up-curl dominated chip, and **f** close-up view of the curled chip

Line CD is the straight major cutting edge of the tool. Since the depth of cut ($a = 0.254$ mm) is smaller than the tool nose radius ($r = 0.8$ mm), the straight cutting edge does not touch the workpiece. As shown in Fig. 9c, the tool contacts the workpiece along the arc AB, which is the chip width. The radii of the workpiece before and after turning are denoted as r_o and r_i, respectively. In this cutting setup, $r_o = 15.93$ mm and $r_i = 15.67$ mm. The cutting speed at points B (with radius r_o) and A (with radius r_i) are 48.8 and 48.0 m/min, respectively. The change of cutting speed along the chip thickness is only 1.6%. The small change in cutting velocity across the chip thickness results in the up-curl dominated pattern, as illustrated in Fig. 9b. The effect of side-curl can also be seen to create the pitch of the curled chip. The tubular type helix chip [35] is formed by rotational and translational motion along an axis parallel to the tool rake face.

The finite element method is applied to simulate the cutting using the right-handed tool. The cutting configuration is shown in Fig. 9d with AB marked the chip width. Y and Z indicate the radial and axial direction of the workpiece, respectively. Figure 9e shows the 15.2 mm length of cut to create the curled chip in 3D finite element simulation. The close-up view of the curled chip is shown in Fig. 9f. Qualitatively, the morphology of the chip curl obtained from experiment (Fig. 9a) and finite element modeling (Fig. 9f) shows a similar pattern. The chip flow direction also matches each other in finite element modeling and

Table 1. Comparison of the radius and pitch in turning CP Ti with 0.254 mm depth of cut, 48.8 m/min cutting speed, 0.254 mm/rev feed, and 0.8 mm tool nose radius

	Radius (mm)	Pitch (mm)
Experiment	2.1–2.7	2.9–3.6
Finite element simulation	1.2	1.5

experimental observation. However, the finite element method under-predicts the radius and pitch of the chip curl by about 50%, as listed in Table 1. One possible cause for this discrepancy is due to the contact of the chip with the tool, tool holder, and/or workpiece during cutting. According to Cook et al. [32], such contact results in a larger chip curl radius. In finite element modeling, such contact does not exist. In actual cutting, such contact is inevitable and will increase the radius and pitch of the curled chip. Another possible cause is due to the external force acting on the chip by the weight of the chip after cutting. Since the chip formation is continuous, the chip is pulled by its own weight to make a larger radius and pitch on the curled chip.

When the depth of cut is increased to 1.02 mm, the washer-type helical chip [35], as shown in Fig. 10a, is observed in the turning experiment. This is different from the tubular chip in Fig. 9a for small depth of cut. As shown in Fig. 10b, such washer-type he-
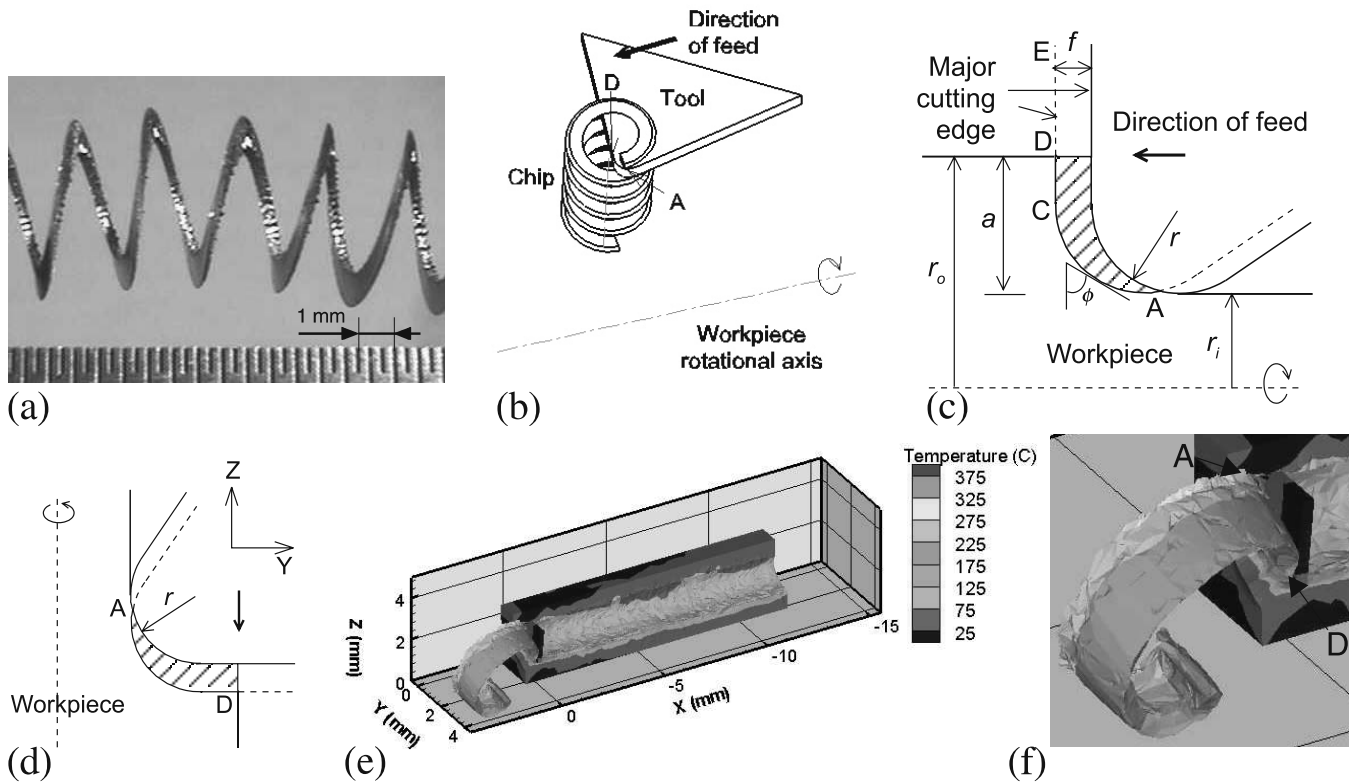
Fig. 10a–f. Chip curl with 1.02 mm depth of cut, 48.8 m/min cutting speed, 0.254 mm/rev feed, and 0.8 mm tool nose radius: **a** washer-type chip in the experiment, **b** side-curl dominated chip, left-handed tool, and rotational axis of workpiece, **c** top view of the left-handed tool and uncut chip cross-section, **d** top view of the right-handed tool and uncut chip cross-section, **e** up-curl dominated chip formation in finite element simulation, and **f** close-up view of the curled chip

lical chip is due to the side-curl of the chip during cutting. Chip side-curl is due to the variation of cutting speed across the chip width, marked by arc AC and line CD in Fig. 10c. Figure 10c shows the top view of the tool and uncut chip cross-section. Since the depth of cut ($a = 1.02$ mm) is bigger than the tool nose radius ($r = 0.8$ mm), the tool contacts the workpiece along the arc AC and line CD. In this cutting configuration, $r_o = 15.93$ mm and $r_i = 14.91$ mm. The cutting speed at points D (with radius r_o) and A (with radius r_i) are 48.8 and 45.6 m/min, respectively. The change of cutting speed along the chip thickness is increased to 6.4%, much larger than the previous small depth of cut condition. Furthermore, the varying local inclination angles, marked as ϕ in Figs. 9 and 10, on the cutting edge varies significantly in the large depth of cut cutting configuration. According to Li et al. [34], the change in ϕ results in the variation in inclination angle for oblique cutting and promotes the chip side-curl.

In finite element modeling, the right-handed tool configuration, as shown in Fig. 10d is used. Figure 10e shows the 12.7 mm length of cut. The curl pattern, as shown in the close-up view in Fig. 10f, is dominated by the up-curl, not the side-curl observed in Figs. 10a and 10b. The main reason for such discrepancy is the lack of variation of cutting speed at points A and D on the tool inner and outer edges. The cutting configuration is the straight-shaping, which neglects the workpiece curvature effect. The 3D finite element method used in this study is adequate to estimate the cutting forces and tool temperature but not suitable for prediction of the chip curl when the variation in cutting speed across the chip width become larger.

7 Chip segmentation with the shear band formation

The Ti chips in this study are segmented with the shear band formation. Due to the low thermal conductivity of Ti, the heat is difficult to transfer outside the deformation zone during the chip formation. The high temperature is confined in the deformation zone, softens the work-material, generates even larger deforma-

tion and heat, and further increases the temperature in a narrow band of the deformation zone. The shear band formation and chip segmentation are the manifestation of the thermo-mechanical instability in the machining process [13]. In recent years, 2D finite element modeling has been applied [14, 15, 21] to study the chip segmentation. To the best of our knowledge, the 3D modeling of chip segmentation with shear band formation in Ti machining has not been investigated, likely due to the extensive computational time and the fine mesh requirement. In this study, the 3D finite element method is applied to investigate the segmented, shear localized chips.

The CP Ti chip machined at 195 m/min cutting speed, 0.254 mm/rev feed, and 1.02 mm depth of cut is examined using the microscope. The side-curl dominated chip, similar to the chip in Fig. 10a, is generated. An optical micrograph of the segmented chip with shear band formation is shown in Fig. 11a. The chip composed of small segments divided by the shear bands. The spacing of these segments, denoted as w_1, w_2, w_3, and w_4, is defined as the distance between the two adjacent shear bands. The spacing varies in the range of 0.19 to 0.32 mm.

The finite element modeling under the same cutting conditions was conducted. Different finite element settings were evaluated to enable the chip to display the segmentation. Two key factors were found to be critical. One is small element size in the workpiece and chip. The automatic mesh refinement is used in the 3D finite element machining modeling. The element size is small at the cutting edge and in the deformation zone due to the high stress gradient. The automatic remeshing increases the element size in the chip after the workpiece passes through the deformation zones. A certain level of small element size must be maintained to retain the sign of element separation due to chip segmentation. Another factor is the small mesh size in the tool tip to model the sharp cutting edge. Machining Ti has a short tool-chip contact length [5]. Fine tool mesh is important to match to the small element size of the workpiece at the cutting edge.

Figure 11b shows the chip morphology of finite element modeling. Four shear bands, displayed as cracks in the chip free

Fig. 11a,b. Segmented chip with 1.02 mm depth of cut, 195 m/min cutting speed, 0.254 mm/rev feed: **a** photomicrograph and **b** finite element simulation
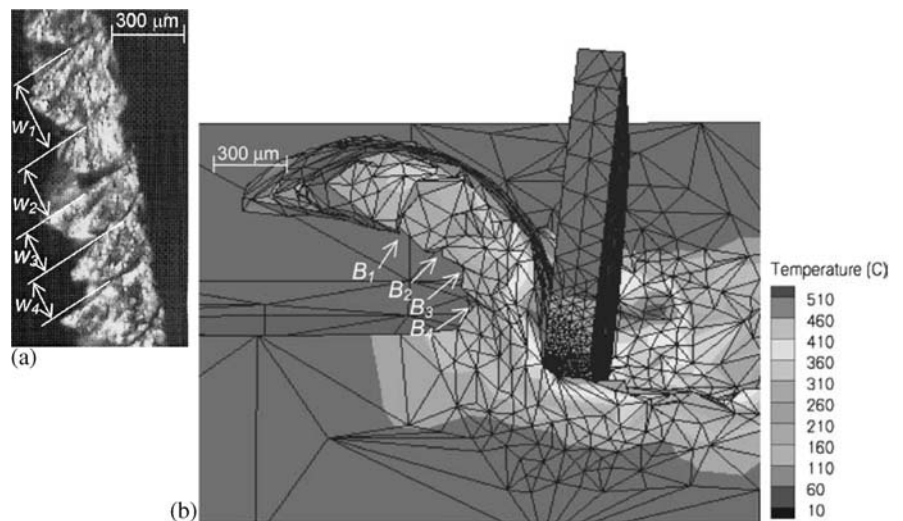
surface, are labeled as B_1, B_2, B_3, and B_4. At the viewing angle in Fig. 11b, the separation of elements at B_1 and B_4 are obvious. By alternating to different viewing directions, the separation of elements at B_2 and B_3 are also apparent. The distance between adjacent shear bands is about 0.18 to 0.25 mm, which is comparable with experimental results.

8 Concluding remarks

The 3D finite element simulation of turning the CP Ti was validated by the comparison of cutting forces and chip thickness with reasonable agreement. Effects of cutting speed on peak tool temperature and tool cutting edge radius on forces, chip thickness, and tool temperature were investigated. The application of finite element simulation to study the chip curl was explored. Qualitative agreement on the type of chip curl and chip flow direction were achieved for turning with small depth of cut. The chip segmentation with shear band formation was investigated. The segment spacing in the finite element modeling was comparable to experimental measurements. The feasibility to use the finite element method to model the complicated 3D machining processes was demonstrated.

This study has also identified several future research directions to expand the scope and improve the accuracy of 3D finite element machining simulation tool. Significant research work is currently on going to study the end-milling of Ti alloys. The finite element modeling can assist the development of new tool materials and coatings for Ti machining. More complicated workpiece modeling, such as the incorporation of the curvature effect, and tool modeling, such as drilling, are necessary to further expand the application of 3D finite element method for machining modeling and productivity improvement.

References

1. Hurless BE, Froes FH (2002) Lowering the cost of titanium. The AMP-TIAC Quarterly 6(2):3–9
2. Kraft EH (2003) Summary of emerging titanium cost reduction technologies. Oak Ridge National Laboratory Report ORNL/Sub/4000023694/1, December 2003
3. Turner PC, Hansen JS (1993) Progress toward low-cost titanium. Adv Mater Process 143(1):42–43
4. Kraft EH (2002) Opportunities for low cost titanium in reduced fuel consumption, improved emission, and enhanced durability heavy-duty vehicles. Oak Ridge National Laboratory Report ORNL/Sub/4000013062/1, July 2002
5. Machado AR, Wallbank J (1990) Machining of titanium and its alloys-a review. Proc Inst Mech Eng, Part B: J Eng Manuf 204:53–60
6. Ezugwu EO, Wang ZM (1997) Titanium alloys and their machinability-a review. J Mater Process Tech 68(1):262–274
7. Yang X, Liu CR (1999) Machining titanium and its alloys. Mach Sci Tech 3(1):107–139
8. Rahman M, Wong YS, Zareena AR (2003) Machininability of titanium alloys. JSME Int J, Series C: Mech Sys, Mach Elem Manuf 46(1):107–115
9. Jones PE, Eylon D (1999) Effects of conventional machining on high cycle fatigue behavior of intermetallic alloy Ti-47Al-2Nb-2Cr (at%). Mat Sci Eng A 263(2):296–304
10. Yang X, Liu CR, Grandt AF (2002) An experimental study on fatigue life variance, residual stress variance, and their correlation of face-turned and ground Ti 6Al-4V. J Manuf Sci Eng 124:809–818
11. Komanduri R, Hou Z (2002) On Thermoplastic shear instability in the machining of a titanium alloy (Ti-6Al-4V). Metall Mat Trans 33(9):2995–3010
12. Sheikh-Ahmad J, Balley JA (1997) Flow instability in the orthogonal machining of CP titanium. J Manuf Sci Eng 119(1):307–312
13. Molinari A, Musquar C, Sutter G (2002) Adiabatic shear banding in high speed machining of Ti-6Al-4V: experiments and modeling. Int J Plast 18:443–459
14. Shivpuri R, Hua J, Mittal P, Srivastava AK (2002) Microstructure-mechanics interactions in modeling chip segmentation during titanium machining. CIRP Ann 51(1):71–74
15. Bäker M (2003) The influence of plastic properties on chip formation. Comp Mat Sci (28):556–562
16. Hong SY, Ding Y, Jeong W (2001) Friction and cutting forces in cryogenic machining of Ti-6Al-4V. Int J Mach Tools Manuf 41:2271–2285
17. Gente A, Hoffmeister H-W (2001) Chip formation in machining Ti6Al4V at extremely high cutting speeds. CIRP Ann 50(1):49–52
18. Norihiko N (2002) High-speed machining of titanium alloy. Chin J Mech Eng 15:109–114
19. Balkrishna R, Shin YC (2002) A study on the high speed face milling of Ti-6Al-4V alloy. 2002 ASME IMECE, New Orleans, LA, MED 13:277–286
20. Corduan N, Himbert T, Poulachon G, Dessoly M, Lambertin M, Vigneau J, Payoux B (2003) Wear mechanism of new tool materials for Ti-6Al-4V high performance machining. CIRP Ann 52(1):73–76
21. Obikawa T, Usui E (1996) Computational machining of titanium alloy - finite element modeling and a few results. J Manuf Sci Eng 118(2):208–215
22. Ehmann KF, Kapoor SG, Devor RE, Lazoglu I (1997) Machining process modeling: a review. J Manuf Sci Eng 119:655–663
23. van Luttervelt CA, Childs T, Jawahir IS, Klocke F, Venuvinod PK (1998) Present situation and future trends in modelling of machining operations. Progress report of the CIRP working group 'modelling of machining operations'. CIRP Ann 48(2):587–626
24. Stephenson DA, Agapiou JS (1996) Metal cutting theory and practice. Dekker, New York
25. Marusich TD, Ortiz M (1995) Modeling and simulation of high-speed machining. Int J Num Meth Eng 38(21):3675–3694
26. Shih AJ (1995) Finite element simulation of orthogonal metal cutting. ASME J Eng Ind 117:84–93
27. ASM Handbook Committee (1978) Metals Handbook: Vol. 2, Properties and selection–nonferrous alloys and pure metals. American Society for Metals, Metals Park, OH
28. ASM Handbook Committee (1978) Metals Handbook: Vol. 3, Properties and selection–stainless steels, tool materials, and special-purpose metals. American Society for Metals, Metals Park, OH
29. Welsh G, Boyer R, Collings EW (eds) (1994) Materials properties handbook: titanium alloys. ASM International, Materials Park, OH
30. Jawahir IS, van Luttervelt CA (1993) Recent developments in chip control research and applications. CIRP Ann 42(2):659–693
31. Fang N (2002) Kinematic characterization of chip lateral-curl - the third pattern of chip curl in machining. J Manuf Sci Eng 124:667–675
32. Cook NH, Jhaveri P, Nayak N (1963) The mechanism of chip curl and its importance in metal cutting. J Eng Ind 85(2):374–380
33. Nakayama K (1978) Basic rules on the form of chip in metal cutting. CIRP Ann 27(1):17–21
34. Li Z, Qu G, Xu Y, Rong Y (1997) Formation and breaking of side-curl dominated short-spiral chips. 1997 ASME IMECE, 16–21 Nov 1997, Dallas, TX, MED 6–2:305–312
35. Boothroyd G, Knight WA (1989) Fundamentals of machining and machine tools. Dekker, New York